Title

Evolution of Cell Size Homeostasis and Growth Rate Diversity during Initial Surface Colonization of Shewanella oneidensis

Journal

ACS Nano, 10(10)

ISSN

1936-0851

Authors

Lee, Calvin K
Kim, Alexander J
Santos, Giancarlo S
et al.

Publication Date

2016-10-25

DOI

10.1021/acsnano.6b05123

Peer reviewed

ACSNANO

www.acsnano.org

ARTICLE

Evolution of Cell Size Homeostasis and Growth Rate Diversity during Initial Surface Colonization of *Shewanella oneidensis*

Calvin K. Lee,[†] Alexander J. Kim,[†] Giancarlo S. Santos,[†] Peter Y. Lai,[†] Stella Y. Lee,[†] David F. Qiao,[†] Jaime De Anda,[†] Thomas D. Young,[‡,§] Yujie Chen,[†,#] Annette R. Rowe,[⊥] Kenneth H. Nealson,[⊥] Paul S. Weiss,[‡,§,∥] and Gerard C. L. Wong*[,†,‡,§]

[†]Department of Bioengineering, [‡]Department of Chemistry & Biochemistry, [§]California NanoSystems Institute, and [∥]Department of Materials Science & Engineering, University of California, Los Angeles, Los Angeles, California 90095, United States

[⊥]Department of Earth Sciences & Biological Sciences, University of Southern California, Los Angeles, California 90089, United States

Supporting Information

ABSTRACT: Cell size control and homeostasis are fundamental features of bacterial metabolism. Recent work suggests that cells add a constant size between birth and division ("adder" model). However, it is not known how cell size homeostasis is influenced by the existence of heterogeneous microenvironments, such as those during biofilm formation. *Shewanella oneidensis* MR-1 can use diverse energy sources on a range of surfaces *via* extracellular electron transport (EET), which can impact growth, metabolism, and size diversity. Here, we track bacterial surface communities at single-cell resolution to show that not only do bacterial motility appendages influence the transition from two- to three-dimensional biofilm growth and control postdivisional cell fates, they strongly impact cell size homeostasis. For every generation, we find that the average growth rate for cells that stay on the surface and continue to divide (nondetaching population) and that for cells that detach before their next division (detaching population) are roughly constant. However, the growth rate distribution is narrow for the nondetaching population, but broad for the detaching population in each generation. Interestingly, the appendage deletion mutants (Δ*pilA*, Δ*mshA-D*, Δ*flg*) have significantly broader growth rate distributions than that of the wild type for both detaching and nondetaching populations, which suggests that *Shewanella* appendages are important for sensing and integrating environmental inputs that contribute to size homeostasis. Moreover, our results suggest multiplexing of appendages for sensing and motility functions contributes to cell size dysregulation. These results can potentially provide a framework for generating metabolic diversity in *S. oneidensis* populations to optimize EET in heterogeneous environments.

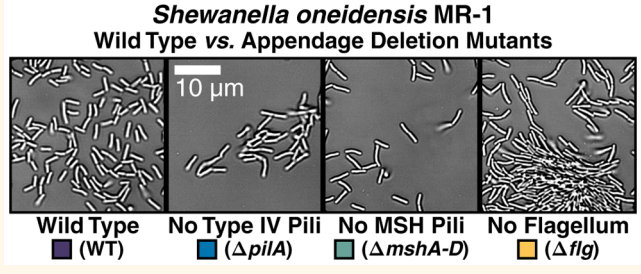

KEYWORDS: *bacteria biofilm communities, single-cell tracking, bacteria microscopy, bacterial appendages, cell size homeostasis, Shewanella oneidensis*

Cell size control and homeostasis are fundamental features of bacterial development and metabolic pathways. Historically, the field of cell size homeostasis has largely depended on single-cell measurements of cellular growth from microscopy images. Recently the advent of microfluidics-based "mother machines" has been able to generate data with the throughput and spatiotemporal resolution required to test previously proposed hypotheses rigorously.[1] These data do not appear to support models in which microbes measure a critical size ("sizer") or a specific time elapsed during the cell cycle ("timer") to trigger division.[1] The emerging picture for homeostasis is based on the "adder" principle of size homeostasis, where all cells under steady-state growth conditions add a nearly constant size between birth and division, independent of their various birth sizes.[1] At present, however, it is not known how cell size homeostasis and associated cellular metabolism are influenced by the existence of heterogeneous microenvironments, such as those during biofilm formation, where each individual bacterium can experience different stimuli and have differential access to nutrients. *Shewanella oneidensis* MR-1 interacts with various surfaces and can utilize diverse energy sources *via* extracellular electron transport (EET). Recent research has led to proposals

Received: July 30, 2016
Accepted: August 29, 2016
Published: August 29, 2016

DOI: 10.1021/acsnano.6b05123
ACS Nano 2016, 10, 9183–9192

of a few strategies for how EET is mediated in these microbial systems, including soluble redox mediators (*e.g.*, flavins) to shuttle electrons *via* diffusion, direct contact with membrane cytochromes to the solid surface, and production of bacterial nanowires to bridge the gap between the cell body and surface.[2−8] These interactions and strategies, which are driven by stress and local scarcity of nutrients in their microenvironment, can affect their growth, metabolism, size diversity, behavior, and the EET process.

In our work, we show that growth rate diversity and dysregulation of cell size homeostasis are influenced by structural features of *S. oneidensis* surface adaptation and sensing *via* its nanoscopic appendages (pili and flagellum). Previous biofilm studies have implicated the importance of appendages in *S. oneidensis* biofilm formation and development.[9−11] Recent work has shown that bacterial appendages can be both effectors and sensors and integrate over environmental inputs.[12−18] However, it is not well known how appendage-related inputs (*e.g.*, sensing) and outputs (*e.g.*, motility) can impact the observed size and behavior diversity of a biofilm population. The ability to monitor the longitudinal evolution of cell size in bacterial communities that develop freely on surfaces and identify factors that influence such evolution requires tools that do not just measure cell size but also capture entire histories of all cells across all generations (motility, division, appendage usage). We use recently developed methods for tracking entire bacterial surface communities with single-cell resolution (a total of up to 1 000 000 snapshots of single bacteria) to show that not only do appendages impact biofilm growth and metabolic behavior through the transition from two-dimensional (2-D) to three-dimensional (3-D) biofilm growth and postdivision cell fates, they strongly impact cell size homeostasis, growth rate, and motility. For every generation, we find that the average growth rates for cells that continue to divide and cells that detach before division (nondetaching population) are roughly constant, consistent with the "adder" model. However, for cells that detach in a given generation (detaching population), the preparation for surface detachment in that generation seems to generate diverse growth rates: the distribution of growth rates is narrow for the cells that continue to divide, but approximately 3× broader for cells that detach. To examine the origins of this effect, we investigate appendage deletion mutants (Δ*pilA*, Δ*mshA-D*, Δ*flg*), which ablate both their motility and sensing functions. The results for the mutants show that the detaching population exhibits a broad range of growth rates as expected, but the nondetaching population surprisingly also exhibits a broad range of growth rates (approximately 2−4× broader). By correlating these growth rate observations with motility measurements from the same cells, we suggest that the multiplexing of sensing and motility functions in appendages contributes to cell size dysregulation. These results provide a framework for understanding diversity of *S. oneidensis* populations during biofilm formation and EET in heterogeneous environments. Moreover, the process of surface sensing in *S. oneidensis via* appendages can inherently drive cell size diversity during biofilm formation and in principle lead to subpopulations with differential EET output, with consequences for bioremediation, electricity generation, and biofuel production.[19]

RESULTS AND DISCUSSION

Appendages Impact Transition from 2-D to 3-D Structural Development in Early *S. oneidensis* MR-1 Biofilms. Metabolic behavior of biofilm development depends on both population-level and single-cell-level effects. For population-level effects, it is important to differentiate between metabolic outcomes that stem from the biofilm morphology, such as changes that occur when cells evolve from 2-D growth (where a monolayer of cells covers progressively more of the surface) to 3-D growth (where cells start to overlap with one another), and those that originate from the process of surface sensing and adaptation, such as changes that occur even during purely 2-D growth. For example, we expect the transition from 2-D to 3-D growth to have a significant baseline influence on the metabolisms of individual cells within the biofilm. As 3-D structures are formed, cells on the inside of the biofilm will have decreased access to nutrients, such as oxygen, in their microenvironment compared to cells on the outside of the biofilm.[20] Moreover, for *S. oneidensis*, it is known that different appendages can contribute differently to the various structural stages of biofilm growth.[9] We examine three types of appendages important for *S. oneidensis* development with their respective structural subunit genetic knockout strains: type IV pili (TFP) with Δ*pilA*, mannose-sensitive hemagglutinin (MSH) pili, with Δ*mshA-D*, and a single polar flagellum with Δ*flg*. Pili appendages are typically used for surface attachment and motility, while flagellum appendages are typically used for swimming, but both appendages can affect surface motility and behavior.[21] These long protein filaments are extremely thin, with their diameters orders of magnitude smaller than their lengths (typical TFP diameter ∼5 nm, typical flagellum diameter ∼20 nm, and length ∼10 μm[22−26]), and cannot be visualized with conventional light microscopy. Previous studies showed that, compared to wild type (WT), cells lacking pili were unable to cover the surface and instead formed towering, densely packed 3-D structures, while cells lacking flagella were unable to form any 3-D structures.[9] Here, we examine how appendages impact the 2-D to 3-D structural development of early stage biofilms.

Figure 1a qualitatively shows the effects of appendage deletion on the transition from 2-D to 3-D growth, and our observations from the recordings are consistent with previous studies of these mutants.[9] To correlate these observations with more quantitative comparisons, we plotted the 2-D surface covered as a function of the number of cells in our field of view and found that these two variables were linearly related while the cells were mostly undergoing 2-D growth (see Figure 1b). Within this linear regime, we could easily compare the effects of appendage deletion on the transition seen in Figure 1a. We defined effective surface coverage as the projected lengths of the fitted lines in Figure 1b onto the *x*-axis (shown as dotted lines), and we reported the value using the number of cells and the calculated surface cell density (number of cells divided by the field of view area). The pili knockouts had much lower effective surface coverage compared to wild type and the flagellum knockout and started forming 3-D structures with much fewer cells. Δ*pilA* had the lowest, with the effective surface coverage at 164 cells or 0.0365 cells/μm^2, which was consistent with our observations of this mutant forming dense 3-D clusters consisting of chains of dividing cells that tended to fold on top of each other. Δ*mshA-D* was slightly higher (208 cells or 0.0463 cells/μm^2), and we observed fewer of those 3-D

DOI: 10.1021/acsnano.6b05123
ACS Nano 2016, 10, 9183−9192

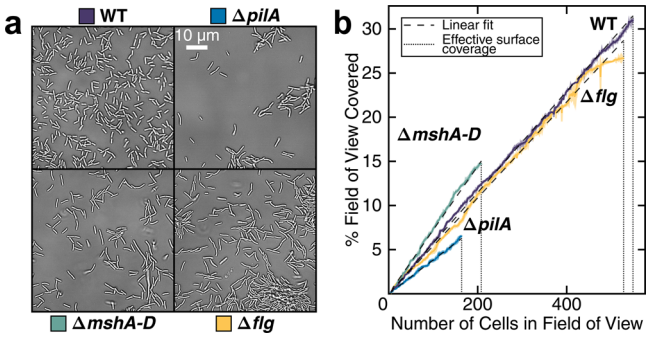

Figure 1. Appendages impact transition from 2-D to 3-D structural development in early *S. oneidensis* MR-1 biofilms. (a) We track the effective surface coverage, or how well the surface is spatially covered, of *S. oneidensis* wild-type and appendage mutants. Representative microscope pictures (field of view is 67 × 67 μm^2) at the end of each data set for each strain: 18.75 h (16 875 frames) for WT, 35 h (31 500 frames) for Δ*pilA*, 37.5 h (33 750 frames) for Δ*mshA-D*, and 35 h (31 500 frames) for Δ*flg*. Scale bar indicates 10 μm. (b) Plot of percent field of view covered *vs* number of cells in field of view. Here, the terminus of each plotted curve indicates the surface cell density and number of cells where the proportion of 2-D surface growth (where a monolayer of cells covers progressively more of the surface) to 3-D growth (where cells start to overlap with one another) decreases below a threshold. Curves represent the mean percent field of view covered for a given number of cells on the surface, shaded areas around the curves indicate ±1 standard deviation (SD), and dashed lines are linear fits of the curves through the origin ([slope, R^2, *p*-value]: WT [0.05735%/cell or 2.574 μm^2/cell, 0.9989, $<10^{-4}$]; Δ*pilA* [0.03822%/cell or 1.716 μm^2/cell, 0.9954, $<10^{-4}$]; Δ*mshA-D* [0.07226%/cell or 3.244 μm^2/cell, 0.9934, $<10^{-4}$]; Δ*flg* [0.05434%/cell or 2.439 μm^2/cell, 0.9970, $<10^{-4}$]). Effective surface coverage is defined as the projected lengths of the fitted lines onto the *x*-axis and is shown as dotted lines (WT [549 cells or 0.122 cells/μm^2]; Δ*pilA* [164 cells or 0.0365 cells/μm^2]; Δ*mshA-D* [208 cells or 0.0463 cells/μm^2]; Δ*flg* [528 cells or 0.118 cells/μm^2]). Both axes are parametrized by time, but when plotting either axis *vs* time, we found it difficult to compare between runs and between strains because cells had a variable lag phase in growth and attached to and detached from the surface throughout the recording.

clusters. WT (549 cells or 0.122 cells/μm^2) and Δ*flg* (528 cells or 0.118 cells/μm^2) both had high effective surface coverage, and 3-D clusters were not observed. Δ*flg* had slightly lower effective surface coverage than WT, and we observed tightly packed clusters of cells that had expanded radially *via* division from a few cells. These tightly packed clusters are also consistent with the fact that Δ*flg* had higher local nematic liquid crystal order (the nematic order parameter *S* is on the order of ∼0.5 *vs* ∼0.3 for the other strains; see Supplementary Figure S1), which indicated that the cells had more ordered, liquid crystalline packing. These results show that, even at the earliest stages of biofilm development, the appendages impact the transition from 2-D to 3-D growth, with the pili having a stronger effect than the flagellum.

Flagella but Not Pili Significantly Impact Postdivision Cell Fates during the First Several Generations on the Surface. Surface sensing is a pivotal event in the developmental trajectory of a biofilm.[18] It is known that cells can attach and detach from a surface, but at present it is not known what events facilitate the net increase of biomass necessary for forming a biofilm on the surface. The prevailing assumption is that bacterial secretion of exopolysaccharides and the concomitant increase in surface adhesion enable this transition. There is an implicit analogy to epitaxial systems in this model. Bacteria, however, are active particles with appendages capable of both sensing and motility. We investigate the initial 2-D growth of bacterial cells, how such growth depends on specific motility appendages, and when cells begin to accumulate on surfaces. In previous work, we showed that the daughter cells' behaviors after a division event can strongly impact microcolony formation.[27] In fact, the postdivision cell fate can impact biofilm development and metabolic behavior at the earliest stages, since surface detachment decreases the surface cell density and is antithetical to biofilm growth. If either one or both of the daughter cells detach from the surface, then the number of surface bacteria that came from division either remains constant or decreases. Previous work has shown that appendages can affect surface detachment.[9,21] Here, we investigated with single-cell resolution precisely how appendages would affect postdivision cell fates and subsequent biofilm development in *S. oneidensis* (see Figure 2).

After a cell divides, its two daughter cells will each have one of two outcomes: the daughter cell will either detach or not detach from the surface during that generation, defined as the time between consecutive division events. (In cases where the recording ends before a given generation of cells divides again, we analyze the time period between the previous division and the end of the recording instead.) We label these two categories as "detaching cells" and "nondetaching cells", respectively. Because we do not differentiate between the two daughter cells, this results in three possible cases of postdivision cell fates: either no daughter cells detaching ($n = 0$), one daughter cell detaching ($n = 1$), or both daughter cells detaching ($n = 2$), where n is the number of daughter cells detaching. We estimated the errors of these proportions using relative error (indicated as the error bars in Figure 2 and calculated as $p/\sqrt{N}$, where p is the proportion and N is the number of division events), and we considered any proportion whose error bar did not overlap with any other error bars a significantly different case. The denominator of the relative error ($1/\sqrt{N}$) gives an estimate on what is considered an unlikely case, which for our data sets are proportions of ≤10%. For all strains, we noticed a small proportion (≤10%) of both daughter cells detaching ($n = 2$), so this case was unlikely for all strains. We observed that for WT there were two dominant cases (∼50% each): no daughter cells detaching ($n = 0$) and one daughter cell detaching ($n = 1$). We also saw that both Δ*pilA* and Δ*mshA-D* behaved similarly to WT (same two dominant cases with statistically similar proportions), which indicated that the pili did not significantly impact postdivision cell fates. Δ*mshA-D* had a slightly smaller proportion (∼40%) of no daughter cells detaching ($n = 0$), but the error bar for this value still touched the error bars for WT and Δ*pilA*, so we treated it as statistically similar. However, for Δ*flg*, we observed a majority (∼80%) of no daughter cells detaching ($n = 0$) and a small proportion (∼10%) of the other two cases ($n = 1$ and $n = 2$), which indicated that if there were no flagella, the majority of cells remained adhered to the surface and that detachments were unlikely. We tested whether any of the four strains were statistically similar or significantly different in terms of the number of daughter cells detaching (n) using unbalanced one-way ANOVA (Kruskal–Wallis test for distribution medians) and multiple comparison tests using Tukey's honest significant difference criterion with a 0.05 significance value. The test showed that WT, Δ*pilA*, and Δ*mshA-D* were statistically similar, while Δ*flg* was statistically

DOI: 10.1021/acsnano.6b05123
ACS Nano 2016, 10, 9183–9192

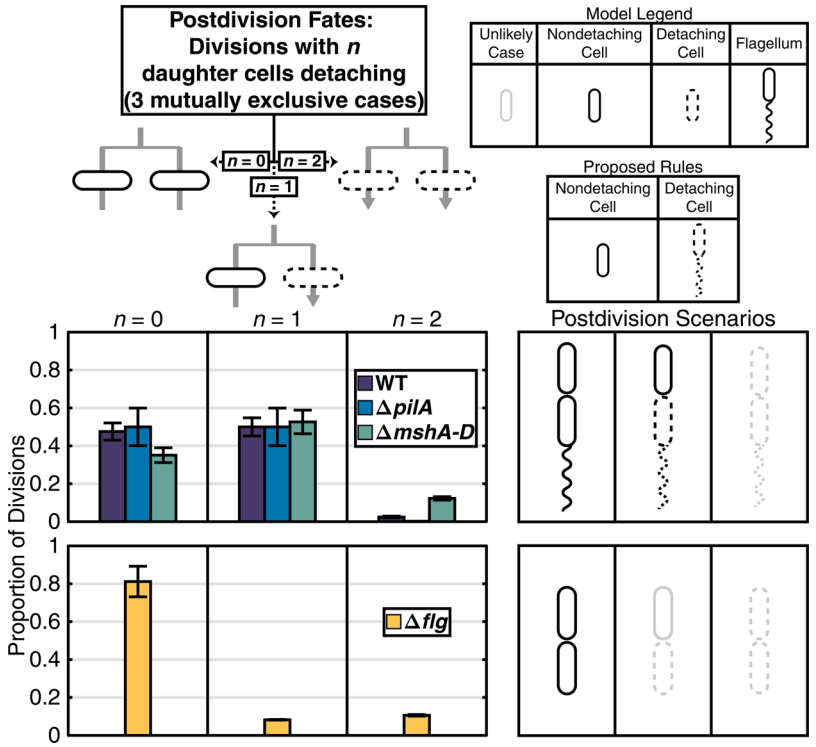

Figure 2. Flagella but not pili significantly impact postdivision cell fates during the first several generations on the surface. Left column shows postdivision observations for each of the studied strains. In WT, Δ*pilA*, and Δ*mshA-D*, most division scenarios result in none ($n = 0$) or one ($n = 1$) of the two daughter cells detaching, with nearly an equal distribution of each. Moreover, the scenario where both daughter cells detach is unlikely. In contrast, the complement is true for the Δ*flg* mutant; both daughter cells remain adhered to the surface, and detachments are unlikely. Control of flagellum activity is critical for regulating the overall population and density of biofilm cells that remain on the surface. Postdivision cell fate is defined as how many of the two daughter cells coming from a division will detach from the surface during that generation. Error bars indicate ±1 relative error (calculated as $p/\sqrt{N}$, where p is the proportion and N is the number of division events). Right column shows the proposed model to rationalize the observations. The daughter cell that inherits the fully developed flagellum from the mother cell detaches from the surface after division, while the daughter cell without the flagellum remains adhered to the surface.

significantly different, which agreed with our observations. These results and the fact that *S. oneidensis* has a single polar flagellum[28] lead us to hypothesize that the flagellum is important for surface detachment.

To test this hypothesis, we used a high-speed camera to capture the detachment sequence of WT *S. oneidensis* (see movie in the Supporting Information). The results in Supplementary Figure S2 show that the cell body of *S. oneidensis* rotates with its long axis normal to the surface at a frequency consistent with the flagellar motor (~20 Hz)[26,29] and culminates in the surface detachment of the cell. The results presented in this section show that the control of flagellum activity can be important for regulating the early 2-D density of biofilm cells that remain on the surface and thereby indirectly affect the landscape for competition. The impact of the flagellum on *S. oneidensis* biofilm development contrasts with that from pili, which do not appreciably impact postdivision cell fates but have a stronger effect on the transition from 2-D to 3-D growth and consequently on differential access of individual cells to nutrients. Interestingly, we find that the largest determinant of individual growth rates is the use of appendages, as described in the next section.

Cells That Detach in a Given Generation Exhibit Diverse Average Growth Rates during That Generation, and Appendage Deletion Mutants Exhibit Dysregulation of Growth Rates. We examine how the use of appendages impacts growth rates of individual cells and cell size homeostasis. To make this determination, we measured average growth rate and other related parameters of single cells on the surface and how detachment and appendages modulated these parameters. We parametrized cell size using the length, since changes in width are negligible from our measurements. To ensure consistent results, we used a single measurement method based on microscopy for all comparisons. Moreover, we calibrated all cell size measurements by imaging *S. oneidensis* WT p519nGFP cells using scanning electron microscopy (SEM) in addition to bright field (BF) light microscopy (see Supplementary Figures S3, S5). This comparison effectively gives us a measurement and error estimate without the typical pixilation-derived sources of error for optical microscopy. As expected, we observed a small difference between the two measurement methods. The mean cell width was 1.10 ± 0.05 μm for cells imaged using BF and 0.92 ± 0.09 μm for cells imaged using SEM. Discrepancies in mean cell width can be attributed to errors in cell size measurements due to the pixel size of the cameras and the image filtering and segmentation process. Due to the inherently different growth conditions for the two measurement techniques and the sensitivity of *S. oneidensis* metabolism to such conditions, we did not attempt to compare the cell lengths using the two techniques. (BF images were taken for cells growing under biofilm conditions on the surface, while SEM images were taken for cells growing under liquid culture conditions.)

To measure growth metrics accurately, we avoid truncation effects by including only bacteria that had their entire lifetime tracked from a division event to either a detachment or

DOI: 10.1021/acsnano.6b05123
ACS Nano 2016, 10, 9183–9192

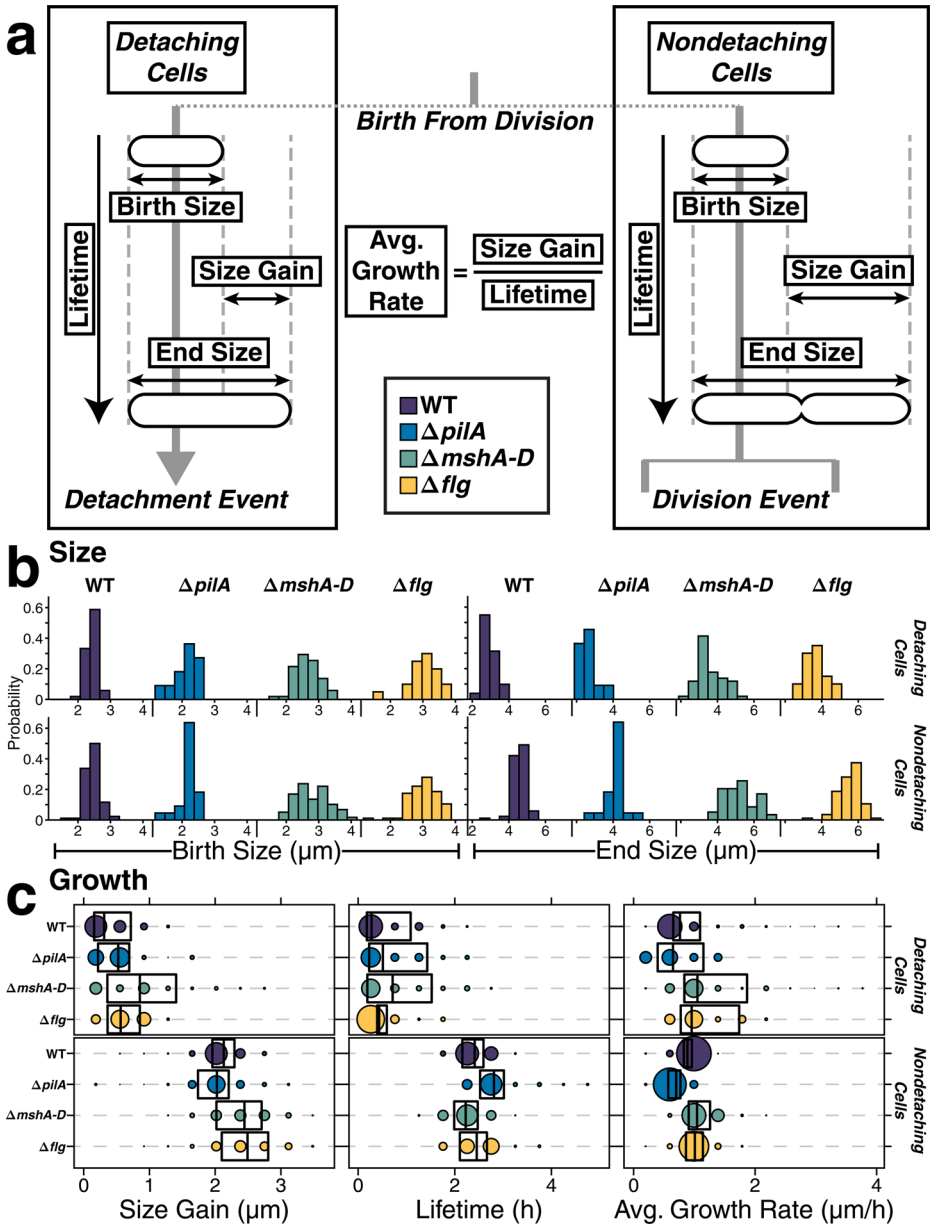

Figure 3. Cells that detach in a given generation exhibit diverse average growth rates during that generation, and appendage deletion mutants exhibit dysregulation of growth rates. (a) Definitions of the single-cell size and growth metrics and their surface behavior categories. These categories, which classify single bacteria, are different from the postdivision cell fates categories, which classify division events. Supplementary Figure S7 shows the relative proportion of bacteria in each of the single-cell categories for each strain. We parametrized cell size using the length, since changes in width are negligible from our measurements. "Lifetime" is defined as the time from birth to either a detachment or division event. "Birth size" is defined as the larger value between the cell size at the frame right after birth and the first percentile of the size distribution during the lifetime. "End size" is defined as the larger value between the cell size at the frame right before the event and the 99th percentile of the size distribution during the lifetime. "Size gain" is defined as end size minus birth size. "Average growth rate" is defined as size gain divided by lifetime. (b) Histograms of size metrics. (c) Histogram box plots of growth metrics. Marker areas are proportional to the probability of events in their respective bins. Boxes indicate 25th (left), 50th (center), and 75th (right) percentiles.

subsequent division event in our categories of "detaching cells" and "nondetaching cells". We tested whether any two categories were statistically similar or significantly different using unbalanced one-way ANOVA (Kruskal–Wallis test for distribution medians) and multiple comparison tests using Tukey's honest significant difference criterion with a 0.05 significance value, the results of which are in Supplementary Tables S1 and S2. We quantified distribution width using interquartile range (IQR), which is defined as the difference between the 75th and 25th percentiles of a distribution, and these values (medians and IQRs) are tabulated in Supplementary Table S3. Note that our definition of average growth rate, which is defined as the size gain divided by the lifetime, is different from the other definition of growth rate, which is defined as the exponent of the length *vs* time function for exponentially growing cells. Finally, we note that the increased motility of detaching cell populations is still quite low and did not contribute significantly to our measurement error. The typical surface speeds of *S. oneidensis* are ∼10 nm/s.

DOI: 10.1021/acsnano.6b05123
ACS Nano 2016, 10, 9183–9192

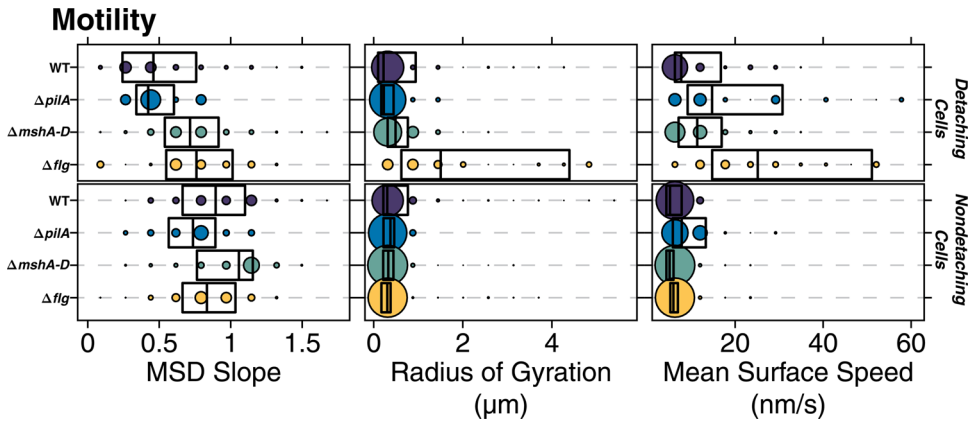

Figure 4. Detaching populations exhibit higher motility than nondetaching populations. Histogram box plots of motility metrics. Marker areas are proportional to the probability of events in their respective bins. Boxes indicate 25th (left), 50th (center), and 75th (right) percentiles. Motility metrics characterize a single cell's trajectory as follows. "Mean squared displacement (MSD) slope" is the slope of the MSD *vs* time delay on a log–log plot and characterizes the directionality of a given trajectory as subdiffusive/immobile motion, diffusive/random motion, or superdiffusive/active motion when the value is less than 1, approximately 1, or greater than 1, respectively. "Radius of gyration" measures the spatial extent of a trajectory and characterizes how much of the surface a given cell traverses laterally. "Mean surface speed" is the total distance traveled (contour length) on the surface divided by the lifetime for a given trajectory.

For a given generation, nondetaching cells were, in general, larger in size at the end of their lifetime and exhibited more size gain. This result was expected because, by definition, they spent more time growing as they stay on the surface until the next division event, whereas detaching cells depart from the surface prematurely before the next division event. Moreover, our measurements show that the birth size and average growth rate distributions for both detaching and nondetaching populations were statistically similar (see Supplementary Table S1). The birth size distribution medians for the detaching and nondetaching populations for WT were 2.43 and 2.45 μm, respectively (Figure 3b column 1), and the average growth rate distribution medians for the detaching and nondetaching populations for WT were 0.76 and 0.89 μm/h, respectively (Figure 3c rows 1 and 5).

Despite the fact that the average growth rate distributions were similar for *S. oneidensis*, we found that the distribution widths were approximately 3× broader in the detaching population compared to the nondetaching population. The average growth rate distribution IQRs for the detaching and nondetaching populations for WT were 0.44 and 0.13 μm/h, respectively (Figure 3c rows 1 and 5). These results show that, compared to the nondetaching population, the detaching population has statistically similar average growth rate distributions, but significantly broader distribution widths.

Even though growth rates, lifetimes, and cell sizes were similar, slight variations in these metrics, as seen by the distribution widths, resulted in desynchronization of cell growth cycles as time progressed and cells divided and thus an observed diversity in cell sizes at any given time point. We illustrate this phenomenon by plotting a growth curve of a representative WT family in Supplementary Figure S6. As time progressed and cells divided, the cell sizes at any given time point (vertical slice through the plot), became more varied, and the growth curves of cells in the next generation diverged further. For example, at the 9 h time point (generation 3), the cell sizes ranged between 2.2 and 2.3 μm. At the 12 h time point (generation 4), the range of cell sizes increased by an order of magnitude (between 2.1 and 3.1 μm). Note that these results are consistent with the "adder" model of cell size homeostasis, since the average growth rates are the same for both detaching and nondetaching populations and the slopes of the growth curves are similar for cells in a given generation. However, there is currently no paradigm for explaining the dysregulation of growth rate for the detaching population.

Broader average growth rate distribution widths suggest several possibilities. One is an effective dysregulation of growth rate that comes from heterogeneous transitions between steady-state surface growth and steady-state planktonic growth. Another is a dysregulation in growth rate and thus cell size homeostasis. In our case, the detaching population suffers a greater degree of such dysregulation than the nondetaching population. We hypothesize that the dysregulation in growth rate for the detaching population is related to sensory input to their appendages, which can be operative in both possibilities. To test this hypothesis, we isolated the effect of detachment and repeated the above comparisons of distribution widths using only the nondetaching population for WT *vs* the appendage deletion mutants (Δ*pilA*, Δ*mshA-D*, Δ*flg*), which impact both their motility and sensing functions. Consistent with our hypothesis, all three of these mutants showed broader average growth rate distribution widths (~2× broader) compared to the WT (see Figure 3c). For the nondetaching population (rows 5–8), the average growth rate distribution IQRs for the four strains (WT, Δ*pilA*, Δ*mshA-D*, Δ*flg*) were 0.13, 0.20, 0.35, and 0.28 μm/h, respectively. These results show that, compared to the WT nondetaching population, the corresponding appendage deletion mutants have significantly broader distribution widths.

When we compared the detaching and nondetaching populations for the appendage deletion mutants (Δ*pilA*, Δ*mshA-D*, Δ*flg*), our data showed that the birth size and average growth rate distributions were statistically similar (see Supplementary Table S1), but the average growth rate distribution widths were approximately 3–4× broader in the detaching population compared to the nondetaching population. This difference is also consistent with our hypothesis on the impact of appendages on size homeostasis. As shown in Figure 3b, the birth size distribution medians for the detaching and nondetaching populations for Δ*pilA* were 2.23 and 2.19 μm, respectively (column 2); for Δ*mshA-D*, 2.59 and 2.75 μm, respectively (column 3); and for Δ*flg*, 3.10 and 3.04 μm,

DOI: 10.1021/acsnano.6b05123
ACS Nano 2016, 10, 9183–9192

respectively (column 4). As shown in Figure 3c, the average growth rate distribution medians for the detaching and nondetaching populations for Δ*pilA* were 0.65 and 0.70 μm/h, respectively (rows 2 and 6); for Δ*mshA-D*, 1.05 and 1.04 μm/h, respectively (rows 3 and 7); and for Δ*flg*, 0.95 and 1.01 μm/h, respectively (rows 4 and 8). As shown in Figure 3c, the average growth rate distribution IQRs for the detaching and nondetaching populations for Δ*pilA* were 0.75 and 0.20 μm/h, respectively (rows 2 and 6); for Δ*mshA-D*, 1.03 and 0.35 μm/h, respectively (rows 3 and 7); and for Δ*flg*, 0.96 and 0.28 μm/h, respectively (rows 4 and 8). Also, our comparison of WT *vs* the appendage deletion mutants using the detaching population shows a drastic broadening of the growth rate distribution widths for the mutants, an observation that also agreed with our hypothesis. For the detaching population (rows 1−4), the average growth rate distribution IQRs for the four strains (WT, Δ*pilA*, Δ*mshA-D*, Δ*flg*) were 0.44, 0.75, 1.03, and 0.96 μm/h, respectively. It is interesting to note that Δ*mshA-D* has the broadest distribution width in both detaching and nondetaching populations, but all three appendage deletion mutants are similar in terms of their broad distribution widths.

Detaching Populations Exhibit Higher Motility than Nondetaching Populations. Appendage usage for surface motility and/or for sensing heterogeneous environments can in principle impact metabolic behavior. For example, motile cells in principle use metabolic overhead to run the flagellum motor[30] and to retract and extend their pili.[14] Cells also use their appendages as the sensors to detect and react to changes in local nutrient availability in their microenvironment.[15,22,31] In this context, we hypothesize that multiplexing used by appendages for sensing and motility contributed to diverse average growth rates. To test this idea, we measured the single-cell surface motility of the different appendage mutants and correlated these metrics to cell size, growth, and detachment metrics for the same corresponding cells for all the cells that we tracked (∼100 cells).

We observed that in general *S. oneidensis* cells on the surface were not very motile, as characterized by several different motility metrics that we use (see Figure 4, Supplementary Tables S1−S3). The general trend was observed for both the detaching and nondetaching populations for WT. Both populations had mean squared displacement (MSD) slope distribution medians less than 1, which indicated that cells moved subdiffusively and did not have any directional preference for lateral movement. Moreover, both populations had radii of gyration smaller than their average cell size by an order of magnitude, which indicated that cells did not exhibit much lateral movement on the surface. Compared to the mean cell length of 3.4 μm, the radius of gyration distribution medians for the detaching and nondetaching populations for WT were 0.22 and 0.30 μm, respectively (Figure 4 rows 1 and 5). The mean surface speed distribution medians for the detaching and nondetaching populations for WT were 7.73 and 5.18 nm/s, respectively (Figure 4 rows 1 and 5). These speeds were ∼5× smaller than that of *Pseudomonas aeruginosa*, a species known to use their appendages for surface motility (∼25 nm/s for WT *P. aeruginosa*).[21]

Having noted the generally low level of motility, we found that the detaching population exhibited significantly more motility than the nondetaching population. We note that this is the same detaching population that shows the greatest dysregulation of growth rates and that this observation is consistent with the hypothesis that the multiplexing of sensing and motility functions in the appendages leads to such dysregulation. For the appendage deletion mutants, the nondetaching population had similar low levels of motility compared to WT. The nondetaching population radius of gyration distribution medians for the three appendage deletion mutants (Δ*pilA*, Δ*mshA-D*, Δ*flg*) were 0.38, 0.33, and 0.30 μm, respectively; mean surface speed distribution medians were 7.85, 5.10, and 5.96 nm/s, respectively (Figure 4 rows 6−8). Consistent with our hypothesis that multiplexing between motility and sensing leads to growth rate dysregulation, we found that the nondetaching mutants had similarly narrow distributions of growth rates compared to WT, presumably due to the low levels of motility activity required for these appendages. On the other hand, the detaching population for the appendage deletion mutants was more varied in the motility metrics. With radius of gyration, the detaching population distribution medians for Δ*pilA* (0.23 μm) and Δ*mshA-D* (0.49 μm) were similar to WT, but Δ*flg* had an order of magnitude greater value (1.50 μm) and a much broader distribution width (3.77 μm *vs* 0.2 to 0.8 μm) (Figure 4 rows 2−4). The detaching population for Δ*pilA* and Δ*flg* had greater mean surface speed distribution medians and widths (Δ*pilA* [median: 14.75 nm/s, IQR: 21.56 nm/s]; Δ*flg* [median: 25.14 nm/s, IQR: 36.32 nm/s]) than Δ*mshA-D* and WT, which were quite similar (Δ*mshA-D* [median: 11.38 nm/s, IQR: 9.79 nm/s]; WT [median: 7.73 nm/s, IQR: 10.44 nm/s]).

Interestingly, specific appendage deletions increased both the mean surface speed distribution medians and widths when comparing the detaching population to the nondetaching population for each of the four strains. This result suggests that some of the appendages have partially antagonistic functions (*e.g.*, adhesion *vs* motility). The mean surface speed distribution medians in Figure 4 for the detaching and nondetaching populations for WT were 7.73 and 5.18 nm/s, respectively (rows 1 and 5); for Δ*pilA*, 14.75 and 7.85 nm/s, respectively (rows 2 and 6); for Δ*mshA-D*, 11.38 and 5.10 nm/s, respectively (rows 3 and 7); and for Δ*flg*, 25.14 and 5.96 nm/s, respectively (rows 4 and 8). The mean surface speed distribution IQRs in Figure 4 for the detaching and nondetaching populations for WT were 10.44 and 3.48 nm/s, respectively (rows 1 and 5); for Δ*pilA*, 21.56 and 7.50 nm/s, respectively (rows 2 and 6); for Δ*mshA-D*, 9.79 and 1.63 nm/s, respectively (rows 3 and 7); and for Δ*flg*, 36.32 and 1.72 nm/s, respectively (rows 4 and 8).

We note, however, that translational speeds on the surface do not seem to determine detachment behavior, at least for WT, Δ*pilA*, and Δ*mshA-D*. From our postdivision cell fate data, all three strains have similar detachment behavior and small radii of gyration (∼0.3 μm), but the translational speeds for the detaching population are different (7.73, 14.75, and 11.38 nm/s for WT, Δ*pilA*, and Δ*mshA-D*). We hypothesize that this similarity is at least in part due to the strong role of the flagellum in determining detachment events. On the other hand, Δ*flg* has a different detachment behavior and significantly higher radius of gyration (1.5 μm *vs* ∼0.3 μm) and mean surface speed (∼25 nm/s *vs* ∼10 nm/s) compared to the other strains. Since the flagellum appears to be used for the vast majority of detachment events, this result likely indicates an alternate detachment mechanism. Consistent with the above, the detaching population is much smaller for Δ*flg* (10−20% of cells and events) than the other strains (30−50% of cells and events) (see Figures 2 and S7).

DOI: 10.1021/acsnano.6b05123
ACS Nano 2016, 10, 9183−9192

Taken together, these intersecting lines of evidence support our hypothesis that multiplexing the appendages for both sensing and motility contribute to diverse growth rates.

Engineering *S. oneidensis* Environmental Sensor Responses to Optimize Extracellular Electron Transport. In the *S. oneidensis* literature, microenvironments and associated micronutrient distributions are thought to be major drivers of EET-related metabolism. Examples of microenvironments and important micronutrients encountered by *S. oneidensis* include oxygen and flavins in biofilm conditions. Oxygen concentration can vary dramatically in biofilms[32] and is likely variable in these systems based on different gradients driven by microbial consumption and replenishment from diffusion of the media.[33] Moreover, flavins have been highlighted as an important microbial metabolite, implicated in respiration[34] and movement,[35] and can likely vary under biofilm conditions as well. The results in this article suggest a complementary approach. By manipulating sensor appendages (exemplified by our deletion mutants), we can alter how *S. oneidensis* senses and metabolically responds to its environment. Results here show that sensor appendage deletion leads to increases in diversity of growth rates with possible metabolic implications. We hypothesize that combining traditional microenvironment manipulation with control of the *S. oneidensis* environmental sensor suite will allow us to engineer communities that have more cells devoted to optimal EET. Interestingly, our hypothesis is consistent with the recent empirical observation that appendage deletion under some conditions leads to increased EET.[36]

CONCLUSIONS AND PROSPECTS

Recently developed methods for tracking entire bacterial surface communities with single-cell resolution have been used to investigate the origins of *S. oneidensis* growth rate diversity and dysregulation of cell size homeostasis. For every generation, we find that while the average growth rate for cells that stay on the surface and continue to divide and that of cells that detach before their next division are roughly constant. The range of observed growth rates is tightly distributed for the cells that continue to divide, but broadly distributed for cells that detach. Further, we find that such diversity in growth rates is strongly influenced by its pili and flagellum appendages. Intersecting lines of evidence support our hypothesis that the multiplexing of sensing and motility functions in appendages contributes to cell size dysregulation. These results provide a framework for controlling and monitoring growth rate and cell size diversity of *S. oneidensis* populations during biofilm formation in heterogeneous environments. It may be possible to control *S. oneidensis* environmental sensor responses (rather than just control the microenvironments) to yield larger subpopulations with optimal EET activity, which in turn can improve their capacity for bioremediation, electricity generation, and biofuel production.[19,37]

METHODS

Strains and Growth Conditions. *Shewanella oneidensis* MR-1 strains wild type with GFP-containing plasmid p519nGFP,[38] pili knockout mutants Δ*pilA* (gene number SO_0417; the gene responsible for encoding pilin A major structural subunit[7]) and Δ*mshA-D* (gene number SO_4103-SO_4105; the gene responsible for encoding MSH pilin structural subunit[39]), and flagellum knockout mutant Δ*flg* (gene number SO_3237-SO_3238; the genes responsible for encoding FliC flagellin structural subunits[36]) were used in this study. All chemicals were purchased from Sigma-Aldrich unless otherwise stated. Strains were cultured in LB broth overnight to stationary phase under shaking (200 rpm) at 30 °C. For cultures with the p519nGFP plasmid, the LB media was supplemented with 50 μg/mL kanamycin. The cells from this culture were pelleted *via* centrifugation at 2300*g* for 5 min, washed twice, and finally resuspended in a chemically defined medium. This medium contained (per liter of deionized water) 15.1 g of PIPES buffer, 3.4 g of sodium hydroxide, 1.5 g of ammonium chloride, 0.1 g of potassium chloride, 0.6 g of sodium phosphate monobasic monohydrate, 18 mM of either sodium L-lactate or sodium DL-lactate as an electron donor, 10 mL of 100× amino acids stock solution, 10 mL of 100× minerals stock solution, and 1 mL of 1000× vitamins stock solution. The 100× amino acids stock solution contained (per liter of deionized water) 2 g of L-glutamic acid, 2 g of L-arginine, and 2 g of DL-serine. The 100× minerals stock solution contained (per liter of deionized water) 1.5 g of nitrilotriacetic acid, 3 g of magnesium sulfate heptahydrate, 0.5 g of manganese sulfate monohydrate, 1 g of sodium chloride, 0.1 g of ferrous sulfate heptahydrate, 0.1 g of calcium chloride dihydrate, 0.1 g of cobalt chloride hexahydrate, 0.13 g of zinc chloride, 10 mg of cupric sulfate pentahydrate, 10 mg of aluminum potassium disulfate dodecahydrate, 10 mg of boric acid, 25 mg of sodium molybdate dihydrate, 24 mg of nickel chloride hexahydrate, and 25 mg of sodium tungstate. The 1000× vitamins stock solution contained (per liter of deionized water) 20 mg of biotin, 20 mg of folic acid, 100 mg of pyridoxine hydrochloride, 50 mg of riboflavin, 50 mg of thiamine hydrochloride, 50 mg of nicotinic acid, 50 mg of D-pantothenic acid hemicalcium salt, 1 mg of vitamin B_{12}, 50 mg of *p*-aminobenzoic acid, and 50 mg of DL-lipoic acid. The medium was adjusted to an initial pH of 7.0 using HCl and NaOH. The culture in this chemically defined medium was grown again overnight to stationary phase ($OD_{600} \approx 1.0$) under shaking at 30 °C. The culture was then diluted to $OD_{600} \approx 0.01$ and injected into a sterile flow cell containing the same chemically defined medium.

Bright Field Microscopy Imaging and Data Acquisition. Flow cells were assembled as previously described[40] and used for all bright field microscopy imaging experiments. After injection into the flow cell, the flow cell was attached to a heating stage set to 30 °C. For time lapse movies, bacteria were incubated without flow for about 10−20 min before starting flow at a volumetric rate of 3 mL/h, and then images were recorded every 4 s per frame using an Andor Neo sCMOS camera, collecting bright field images (image size of 67 × 67 μm^2 or 2048 × 2048 pixels) with a 100× oil objective and a 2× multiplier lens on an Olympus IX83 microscope equipped with a zero drift correction autofocus system. For high-speed movies, no flow was started, and images were recorded immediately after injection at 200 frames per second using a Phantom V12.1 high-speed camera (Vision Research) with an image size of 512 × 512 pixels (0.1 μm/pixel size) using the same microscope setup.

As previously described, oxygen becomes limited at the flow cell coverslip surface, even with aerobic medium, above a threshold surface cell density and distance from the inlet.[7] This is due to laminar flow (no mixing between adjacent fluid layers) and the no-slip boundary condition (zero fluid velocity at the surface). We adapt the calculation performed previously[7] and replace their reported conditions with our relevant conditions. Flow cell channel dimensions are length L = 40 mm, width w = 4 mm, and height d = 1 mm. Volumetric flow rate is Q = 3 mL/h or 0.833 μL/s, and average fluid velocity is $\bar{v}$ = 0.625 μm/s at a surface fluid layer thickness h = 1 μm. Reynolds number (based on channel dimensions and fluid flow of a rectangular cross-sectional pipe) is Re = 0.3745, which is in the laminar flow regime. Oxygen consumption rate is $\alpha = 7.694 \times 10^{-2}$ mg/L/s at a surface cell density of 10 cells per 67 × 67 μm^2 field of view (lower limit estimate) and an estimated cellular electron transfer rate of 2.6×10^6 e^-/cell/s.[4] Inlet oxygen concentration remains unchanged from their reported value. With these values, our calculations show that the surface fluid layer should start being oxygen limited at a distance of 65 μm from the inlet, which is orders of magnitude closer to the inlet than our imaging location (~20 mm from the inlet). Oxygen limitation has been previously reported to occur within 2 h after bacteria injection,[7] and

DOI: 10.1021/acsnano.6b05123
ACS Nano 2016, 10, 9183−9192

we record for an order of magnitude longer (12−36 h). Also, the laminar flow condition should hold as long as the cells are mostly undergoing 2-D growth, which is our analysis window. Therefore, we assume that the microenvironment for cells on the surface is oxygen limited during our recordings.

Scanning Electron Microscopy Imaging. MR-1 p519nGFP cells were cultured using the same conditions for LB. The centrifugation step was the same, except the chemically defined medium was also supplemented with FM 4-64FX membrane stain and 30 mM dibasic sodium fumarate. The washed cells were incubated at 32 °C in closed containers for 2.5 h under shaking. Cells were centrifuged one time, the medium was replaced with 2.5% glutaraldehyde in phosphate-buffered saline (pH 7.2, 155.17 mM NaCl, 1.54 mM KH_2PO_4, 2.71 mM Na_2HPO_4 $7H_2O$), and the cells were incubated in the glutaraldehyde solution for 2.5 h. Then, cells were centrifuged twice and resuspended in deionized water. The fixed cells were suspended above a flame-annealed 100 nm gold surface (gold was supported on a silicon chip with a 5 nm thick titanium adhesion layer) for 2 h. The substrate was removed and submerged in fresh deionized water. The sample was then removed from the water and dried with a stream of N_2. A JEOL JSM-6700F field emission SEM was used to image cells with an SEI secondary electron detector. A 15 kV accelerating voltage was applied at 10 μA emission. Working distance was set to 8 mm.

Image and Data Analysis. Analyses of these recordings start when cells start moving or growing on the surface, which can be either the actual recording start time or later depending on whether the cells on the surface have a lag phase. Analyses end (15 000−35 000 frames) when either the area covered by cells is overlapping or growing in the direction normal to the surface, which greatly reduces accuracy in segmentation, tracking, and determining single cell metrics, is greater than a determined proportion of the total population surface coverage (see Figure 1b) or the total number of tracked cells gets too large. As a result, each data set can have a variable amount of images analyzed with a total of up to 1 000 000 snapshots of single bacteria. Images were analyzed using a combination of software and algorithms adapted from the methods described[12,27,41] and written in MATLAB R2015a (Mathworks). Supplementary Figure S4 summarizes the image processing and analysis steps. Before generating the binary image *via* Otsu thresholding, the images were further preprocessed and filtered using two edge detection filters, one to re-enhance the bacteria septa and edges between adjacent bacteria and one to re-enhance the bright inner part of bacteria, and then, for bright field images, resized from 2048 × 2048 to 1024 × 1024 pixels, such that the pixel size was 0.065 μm/pixel. For bright field images, the true cell boundaries and sizes are underestimated by image filtering and segmentation because only the inside of the cell is captured. To account for this, the binary image of a single cell was dilated using a disk of radius 5 pixels. After that, the resulting shape was fit to a spherocylinder (union of rectangle and two semicircles). For a spherocylinder, the perimeter was the perimeter calculated from the dilated pixels, the width was the mean value for a single identity calculated by the minor axis of the best-fit ellipse to the dilated pixels, and the length was calculated from the perimeter and width using the geometry formula (see Supplementary Figure S4). Because cell widths were relatively constant for all strains (see Supplementary Figure S3a,b), between imaging modalities (see Supplementary Figure S5), and had greater relative error due to fixed pixel noise, cell sizes were represented by the length. The dilation step added a fixed amount to all calculated widths and lengths, but the calculated size gains and average growth rates were independent of the amount added. For all cells, the growth rates were relatively constant throughout the majority of their lifetimes (see Supplementary Figure S3c), so growth rates could be summarized with just the mean. Mean squared displacement calculations were done using a third-party downloaded MATLAB toolbox.[42] Built-in MATLAB statistical test functions from the Statistics and Machine Learning Toolbox were used for linear fits, unbalanced one-way ANOVA (Kruskal−Wallis test for distribution medians), and multiple comparison tests using Tukey's honest significant difference criterion. *p*-Values for the linear fits were calculated using Monte Carlo bootstrapping methods in MATLAB with random sampling of the data (10 000 iterations, 1000 random sample number, 0.05 significance value). Local nematic order was calculated as previously described,[43] except in 2-D. The local vicinity is defined as a circle, not a sphere, of radius *r*, with a radius of 50 μm corresponding to global order.

ASSOCIATED CONTENT

Supporting Information

The Supporting Information is available free of charge on the ACS Publications website at DOI: 10.1021/acsnano.6b05123.

Figures showing local nematic order; representative movie of *S. oneidensis* detachment process from the surface; cell width distributions and ensemble growth curves; details of determining cell size (length) $L(t)$; SEM images of *S. oneidensis*; growth curve of representative *S. oneidensis* family; proportions of detaching and nondetaching populations; statistical comparisons of metrics between detaching and non-detaching cells for each strain; statistical comparisons of metrics between strains for detaching and nondetaching cells; medians and interquartile ranges of metrics for detaching and nondetaching cells for each strain (PDF)
Video (AVI)

AUTHOR INFORMATION

Corresponding Author

*E-mail: gclwong@seas.ucla.edu.

Present Address

[#]Department of Systems, Synthetic and Physical Biology, Rice University, Houston, Texas 77005, United States.

Notes

The authors declare no competing financial interest.

ACKNOWLEDGMENTS

We acknowledge support from the Office of Naval Research grant N000141410051. We would like to thank M. Ding, H. Y. Shiu, S. L. Li, S. Pirbadian, and M. El-Naggar for their insight and assistance in optimizing cell growth and experiment conditions.

REFERENCES

(1) Taheri-Araghi, S.; Bradde, S.; Sauls, J. T.; Hill, N. S.; Levin, P. A.; Paulsson, J.; Vergassola, M.; Jun, S. Cell-Size Control and Homeostasis in Bacteria. *Curr. Biol.* **2015**, *25*, 385−391.

(2) Gorby, Y. A.; Yanina, S.; McLean, J. S.; Rosso, K. M.; Moyles, D.; Dohnalkova, A.; Beveridge, T. J.; Chang, I. S.; Kim, B. H.; Kim, K. S.; Culley, D. E.; Reed, S. B.; Romine, M. F.; Saffarini, D. A.; Hill, E. A.; Shi, L.; Elias, D. A.; Kennedy, D. W.; Pinchuk, G.; Watanabe, K.; et al. Electrically Conductive Bacterial Nanowires Produced by *Shewanella oneidensis* Strain MR-1 and Other Microorganisms. *Proc. Natl. Acad. Sci. U. S. A.* **2006**, *103*, 11358−11363.

(3) von Canstein, H.; Ogawa, J.; Shimizu, S.; Lloyd, J. R. Secretion of Flavins by *Shewanella* Species and Their Role in Extracellular Electron Transfer. *Appl. Environ. Microbiol.* **2008**, *74*, 615−623.

(4) El-Naggar, M. Y.; Wanger, G.; Leung, K. M.; Yuzvinsky, T. D.; Southam, G.; Yang, J.; Lau, W. M.; Nealson, K. H.; Gorby, Y. a. Electrical Transport along Bacterial Nanowires from *Shewanella oneidensis* MR-1. *Proc. Natl. Acad. Sci. U. S. A.* **2010**, *107*, 18127−18131.

(5) Roy, J. N.; Luckarift, H. R.; Lau, C.; Falase, A.; Garcia, K. E.; Ista, L. K.; Chellamuthu, P.; Ramasamy, R. P.; Gadhamshetty, V.; Wanger, G.; Gorby, Y. A.; Nealson, K. H.; Bretschger, O.; Johnson, G. R.; Atanassov, P. A Study of the Flavin Response by *Shewanella* Cultures in Carbon-Limited Environments. *RSC Adv.* **2012**, *2*, 10020−10027.

DOI: 10.1021/acsnano.6b05123
ACS Nano 2016, 10, 9183−9192

(6) Okamoto, A.; Nakamura, R.; Nealson, K. H.; Hashimoto, K. Bound Flavin Model Suggests Similar Electron-Transfer Mechanisms in *Shewanella* and *Geobacter*. *ChemElectroChem* **2014**, *1*, 1808−1812.
(7) Pirbadian, S.; Barchinger, S. E.; Leung, K. M.; Byun, H. S.; Jangir, Y.; Bouhenni, R. a.; Reed, S. B.; Romine, M. F.; Saffarini, D. a.; Shi, L.; Gorby, Y. a.; Golbeck, J. H.; El-Naggar, M. Y. *Shewanella oneidensis* MR-1 Nanowires are Outer Membrane and Periplasmic Extensions of the Extracellular Electron Transport Components. *Proc. Natl. Acad. Sci. U. S. A.* **2014**, *111*, 12883−12888.
(8) Ding, M.; Shiu, H.-Y.; Li, S.-L.; Lee, C. K.; Wang, G.; Wu, H.; Weiss, N. O.; Young, T. D.; Weiss, P. S.; Wong, G. C. L.; Nealson, K. H.; Huang, Y.; Duan, X. Nanoelectronic Investigation Reveals the Electrochemical Basis of Electrical Conductivity in *Shewanella* and *Geobacter*. Submitted.
(9) Thormann, K. M.; Saville, R. M.; Shukla, S.; Pelletier, D. A.; Spormann, A. M. Initial Phases of Biofilm Formation in *Shewanella oneidensis* MR-1. *J. Bacteriol.* **2004**, *186*, 8096−8104.
(10) Thormann, K. M.; Saville, R. M.; Shukla, S.; Spormann, A. M. Induction of Rapid Detachment in *Shewanella oneidensis* MR-1 Biofilms. *J. Bacteriol.* **2005**, *187*, 1014−1021.
(11) Thormann, K. M.; Duttler, S.; Saville, R. M.; Hyodo, M.; Shukla, S.; Hayakawa, Y.; Spormann, A. M. Control of Formation and Cellular Detachment from *Shewanella oneidensis* MR-1 Biofilms by Cyclic di-GMP. *J. Bacteriol.* **2006**, *188*, 2681−2691.
(12) Gibiansky, M. L.; Conrad, J. C. J. C.; Jin, F.; Gordon, V. D. V. D.; Motto, D. A.; Mathewson, M. A.; Stopka, W. G.; Zelasko, D. C.; Shrout, J. D.; Wong, G. C. L. Bacteria Use Type IV Pili to Walk Upright and Detach from Surfaces. *Science* **2010**, *330*, 197.
(13) Jin, F.; Conrad, J. C.; Gibiansky, M. L.; Wong, G. C. Bacteria Use Type-IV Pili to Slingshot on Surfaces. *Proc. Natl. Acad. Sci. U. S. A.* **2011**, *108*, 12617−12622.
(14) Burrows, L. L. *Pseudomonas aeruginosa* Twitching Motility: Type IV Pili in Action. *Annu. Rev. Microbiol.* **2012**, *66*, 493−520.
(15) Tuson, H. H.; Weibel, D. B. Bacteria-Surface Interactions. *Soft Matter* **2013**, *9*, 4368−4380.
(16) Luo, Y.; Zhao, K.; Baker, A. E.; Kuchma, S. L.; Coggan, K. A.; Wolfgang, M. C.; Wong, G. C. L.; O'Toole, G. A. A Hierarchical Cascade of Second Messengers Regulates *Pseudomonas aeruginosa* Surface Behaviors. *mBio* **2015**, *6*, 1−11.
(17) Persat, A.; Inclan, Y. F.; Engel, J. N.; Stone, H. A.; Gitai, Z. Type IV Pili Mechanochemically Regulate Virulence Factors in *Pseudomonas aeruginosa*. *Proc. Natl. Acad. Sci. U. S. A.* **2015**, *112*, 7563−7568.
(18) O'Toole, G. A.; Wong, G. C. Sensational Biofilms: Surface Sensing in Bacteria. *Curr. Opin. Microbiol.* **2016**, *30*, 139−146.
(19) Kowalchuk, G. A.; Jones, S. E.; Blackall, L. L. Microbes Orchestrate Life on Earth. *ISME J.* **2008**, *2*, 795−796.
(20) Liu, J.; Prindle, A.; Humphries, J.; Gabalda-Sagarra, M.; Asally, M.; Lee, D.-y. D.; Ly, S.; Garcia-Ojalvo, J.; Suel, G. M. Metabolic Co-Dependence Gives Rise to Collective Oscillations Within Biofilms. *Nature (London, U. K.)* **2015**, *523*, 550−554.
(21) Conrad, J. C.; Gibiansky, M. L.; Jin, F.; Gordon, V. D.; Motto, D. a.; Mathewson, M. a.; Stopka, W. G.; Zelasko, D. C.; Shrout, J. D.; Wong, G. C. L. Flagella and Pili-Mediated Near-Surface Single-Cell Motility Mechanisms in *P. aeruginosa*. *Biophys. J.* **2011**, *100*, 1608−1616.
(22) Hammond, S. M.; Lambert, P. A.; Rycroft, A. N. Surface Appendages: Flagella and Fimbriae. In *The Bacterial Cell Surface*; Springer: Dordrecht, The Netherlands, 1984; pp 119−146.
(23) Krogfelt, K. A. Bacterial Adhesion: Genetics, Biogenesis, and Role in Pathogenesis of Fimbrial Adhesins of *Escherichia coli*. *Clin. Infect. Dis.* **1991**, *13*, 721−735.
(24) Biais, N.; Higashi, D. L.; Brujić, J.; So, M.; Sheetz, M. P. Force-Dependent Polymorphism in Type IV Pili Reveals Hidden Epitopes. *Proc. Natl. Acad. Sci. U. S. A.* **2010**, *107*, 11358−11363.
(25) Spagnolie, S. E.; Lauga, E. Comparative Hydrodynamics of Bacterial Polymorphism. *Phys. Rev. Lett.* **2011**, *106*, 058103.
(26) Bennett, R. R.; Lee, C. K.; De Anda, J.; Nealson, K. H.; Yildiz, F. H.; O'Toole, G. A.; Wong, G. C. L.; Golestanian, R. Species-Dependent Hydrodynamics of Flagellum-Tethered Bacteria in Early Biofilm Development. *J. R. Soc., Interface* **2016**, *13*, 20150966.
(27) Zhao, K.; Tseng, B. S.; Beckerman, B.; Jin, F.; Gibiansky, M. L.; Harrison, J. J.; Luijten, E.; Parsek, M. R.; Wong, G. C. L. Psl Trails Guide Exploration and Microcolony Formation in *Pseudomonas aeruginosa* Biofilms. *Nature (London, U. K.)* **2013**, *497*, 388−391.
(28) Paulick, A.; Koerdt, A.; Lassak, J.; Huntley, S.; Wilms, I.; Narberhaus, F.; Thormann, K. M. Two Different Stator Systems Drive a Single Polar Flagellum in *Shewanella oneidensis* MR-1. *Mol. Microbiol.* **2009**, *71*, 836−850.
(29) Sowa, Y.; Hotta, H.; Homma, M.; Ishijima, A. Torque−speed Relationship of the Na^+-driven Flagellar Motor of *Vibrio alginolyticus*. *J. Mol. Biol.* **2003**, *327*, 1043−1051.
(30) Brown, M. T.; Delalez, N. J.; Armitage, J. P. Protein Dynamics and Mechanisms Controlling the Rotational Behaviour of the Bacterial Flagellar Motor. *Curr. Opin. Microbiol.* **2011**, *14*, 734−740.
(31) Armitage, J. P.; Scott, K. A. Bacterial Behavior. In *The Prokaryotes: Prokaryotic Communities and Ecophysiology*; Rosenberg, E.; DeLong, E. F.; Lory, S.; Stackebrandt, E.; Thompson, F., Eds.; Springer: Berlin, Heidelberg, 2013; pp 289−316.
(32) Saville, R. M.; Rakshe, S.; Haagensen, J. A. J.; Shukla, S.; Spormann, A. M. Energy-Dependent Stability of *Shewanella oneidensis* MR-1 Biofilms. *J. Bacteriol.* **2011**, *193*, 3257−3264.
(33) Teal, T. K.; Lies, D. P.; Wold, B. J.; Newman, D. K. Spatiometabolic Stratification of *Shewanella oneidensis* Biofilms. *Appl. Environ. Microbiol.* **2006**, *72*, 7324−7330.
(34) Marsili, E.; Baron, D. B.; Shikhare, I. D.; Coursolle, D.; Gralnick, J. A.; Bond, D. R. *Shewanella* Secretes Flavins that Mediate Extracellular Electron Transfer. *Proc. Natl. Acad. Sci. U. S. A.* **2008**, *105*, 3968−3973.
(35) Li, R.; Tiedje, J. M.; Chiu, C.; Worden, R. M. Soluble Electron Shuttles Can Mediate Energy Taxis toward Insoluble Electron Acceptors. *Environ. Sci. Technol.* **2012**, *46*, 2813−2820.
(36) Bouhenni, R. A.; Vora, G. J.; Biffinger, J. C.; Shirodkar, S.; Brockman, K.; Ray, R.; Wu, P.; Johnson, B. J.; Biddle, E. M.; Marshall, M. J.; Fitzgerald, L. A.; Little, B. J.; Fredrickson, J. K.; Beliaev, A. S.; Ringeisen, B. R.; Saffarini, D. A. The Role of *Shewanella oneidensis* MR-1 Outer Surface Structures in Extracellular Electron Transfer. *Electroanalysis* **2010**, *22*, 856−864.
(37) Rabaey, K.; Rozendal, R. A. Microbial Electrosynthesis - Revisiting the Electrical Route for Microbial Production. *Nat. Rev. Microbiol.* **2010**, *8*, 706−716.
(38) McLean, J. S.; Majors, P. D.; Reardon, C. L.; Bilskis, C. L.; Reed, S. B.; Romine, M. F.; Fredrickson, J. K. Investigations of Structure and Metabolism within *Shewanella oneidensis* MR-1 Biofilms. *J. Microbiol. Methods* **2008**, *74*, 47−56.
(39) Fitzgerald, L. A.; Petersen, E. R.; Ray, R. I.; Little, B. J.; Cooper, C. J.; Howard, E. C.; Ringeisen, B. R.; Biffinger, J. C. *Shewanella oneidensis* MR-1 Msh Pilin Proteins are Involved in Extracellular Electron Transfer in Microbial Fuel Cells. *Process Biochem. (Oxford, U. K.)* **2012**, *47*, 170−174.
(40) Tolker-Nielsen, T.; Sternberg, C. Growing and Analyzing Biofilms in Flow Chambers. In *Current Protocols in Microbiology*; John Wiley & Sons, Inc., 2005.
(41) Utada, A. S.; Bennett, R. R.; Fong, J. C. N.; Gibiansky, M. L.; Yildiz, F. H.; Golestanian, R.; Wong, G. C. L. *Vibrio cholerae* Use Pili and Flagella Synergistically to Effect Motility Switching and Conditional Surface Attachment. *Nat. Commun.* **2014**, *5*, 4913.
(42) Tarantino, N.; Tinevez, J.-Y.; Crowell, E. F.; Boisson, B.; Henriques, R.; Mhlanga, M.; Agou, F.; Israël, A.; Laplantine, E. TNF and IL-1 Exhibit Distinct Ubiquitin Requirements for Inducing NEMO−IKK Supramolecular Structures. *J. Cell Biol.* **2014**, *204*, 231−245.
(43) Drescher, K.; Dunkel, J.; Nadell, C. D.; van Teeffelen, S.; Grnja, I.; Wingreen, N. S.; Stone, H. A.; Bassler, B. L. Architectural Transitions in *Vibrio cholerae* Biofilms at Single-Cell Resolution. *Proc. Natl. Acad. Sci. U. S. A.* **2016**, *113*, E2066−E2072.

DOI: 10.1021/acsnano.6b05123
ACS Nano 2016, 10, 9183−9192